

Vegetation Mapping for Landmine Detection Using Long Wave Hyperspectral Imagery

Alina Zare, Jeremy Bolton, Paul Gader *Senior Member, IEEE*, Miranda Schatten

Abstract—We develop a vegetation mapping method using Long Wave HyperSpectral Imagery (LWHSI) and apply it to landmine detection. The novel aspect of the method is that it makes use of emissivity skewness. The main purpose of vegetation detection for mine detection is to minimize false alarms. Vegetation such as round bushes may be mistaken as mines by mine detection algorithms, especially in Synthetic Aperture Radar (SAR) imagery. We employ an unsupervised vegetation detection algorithm that exploits statistics of emissivity spectra of vegetation in the long wave infrared (LWIR) spectrum for identification. This information is incorporated into a Choquet integral based fusion structure which fuses detector outputs from HyperSpectral Imagery (HSI) and SAR imagery. Vegetation mapping is shown to improve mine detection results over a variety of images and fusion models.

Index Terms— Clustering, Expectation Maximization, Vegetation mapping, Blackbody, Emissivity Normalization, Mine detection, Multisensor systems, Decision level fusion.

I. INTRODUCTION

This paper demonstrates the usefulness of emissivity skewness in vegetation mapping for Long Wave HyperSpectral Imagery (LWHSI). Previously, employing emissivity skewness for vegetation mapping had not been considered. In this paper, vegetation mapping algorithms for the long wave infrared (LWIR) are developed with and without the use of emissivity skewness information. The use of emissivity skewness is supported with examples and experiments that show that its use assists a landmine detection fusion process in distinguishing between landmines and vegetation. The incorporation of the vegetation mapping methods into multi-algorithm, multi-sensor fusion process is briefly described.

The appeal of vegetation detection in the LWIR (8 to 12 microns) is that the imagers can be flown day or night. Furthermore, the LWIR can be used detect buried landmines. Although there are many well known vegetation mapping methods in the visible and near-infrared, the imagers for these wavelengths cannot be flown at night and have more difficulty in detecting buried landmines.

The developed vegetation mapping method is applied to a landmine detection problem involving fusion of LWHSI and Synthetic Aperture Radar (SAR) imagery. Buried mines are most apparent in the LWHSI whereas surface mines are most apparent in the SAR imagery. However, SAR will also give high returns for vegetation. Since the size of a landmine and vegetation in the image could be similar, vegetation could be mistaken for a surface mine by the detectors applied to the radar imagery. Confusion between landmines and vegetation

increases the number of false alarms. Therefore, a vegetation mapping method can be used reduce the number of false alarms caused by vegetation.

The paper is organized as follows. Section II includes discussion on the observed properties of the vegetation and landmine emissivity spectra and emissivity calculations. In Section III, the vegetation mapping algorithm is defined. In Section IV, we briefly discuss the detection algorithms used in fusion. Section V states the fusion method used and Section VI describes the data. Experimental results are given in Section VII. Finally, conclusions and future work are discussed in Section VIII.

II. EMISSIVITY

A. Emissivity Statistics for Vegetation Detection

Detecting vegetation in the thermal infrared depends on the ability to accurately measure emissivity and surface temperature. Vegetation's emissivity spectra (emissivity as a function of wavelength) behave similar to those of a blackbody by having high mean emissivity and a low standard deviation of emissivity across spectral bands [1]. The literature also indicates that vegetation tends to have a lower surface temperature [2]. Therefore, vegetation in a scene can be found by searching for pixels with either low surface temperatures or emissivity spectra that behaves like a blackbody. In this paper, we develop and evaluate a vegetation mapping method using only the emissivity spectra. In particular, we focus on the statistics of emissivity spectra over wavelength.

Figure 1 shows the average emissivity of mines and vegetation for a LWIR image at each wavelength. The average and standard deviations of the emissivity spectra are calculated over the groups of mine and vegetation pixels in the image. As shown in the figure, the vegetation emissivity is high and fairly constant as a function of wavelength when compared to the mine emissivity. Hence, vegetation emissivity spectra exhibit high means and low standard deviations over wavelength. The high mean and low standard deviation of emissivity is characteristic of vegetation and blackbody-like objects. In addition, we observe that the vegetation emissivity spectrum has a left tail and, therefore, has negative skewness over wavelength. The skewness of the vegetation spectrum in Figure 1 is -0.16 whereas the skewness for the mine spectrum is 0.48. In this paper, we show that the mean, standard deviation, and skewness of emissivity spectra over wavelength can be useful in vegetation mapping in LWHSI. Previously, emissivity skewness has not been considered.

Further evidence that emissivity skewness can distinguish vegetation is shown in Figure 2. Figure 2 displays histograms of emissivity skewness values over wavelength for mine and vegetation pixels selected from our data. These histograms show that the distribution of emissivity skewness values for vegetation pixels is primarily negative whereas mine values are primarily positive.

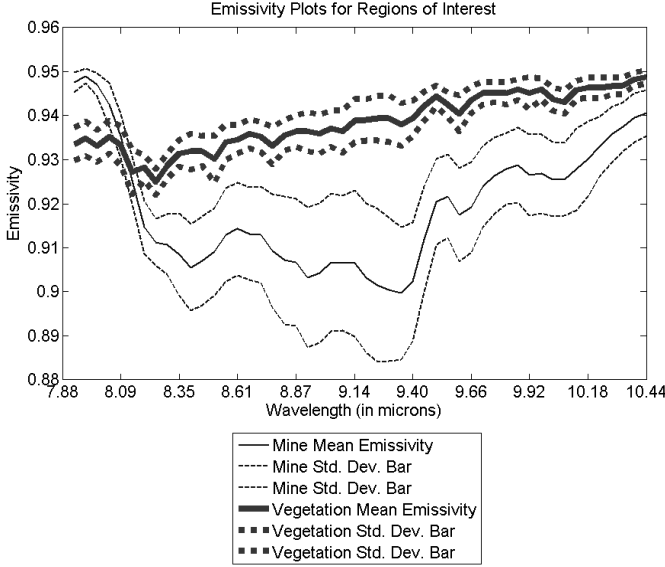


Figure 1. Emissivity Plots for Mine and Vegetation Regions. The means and standard deviations in the plot were taken over multiple spatial samples; these were not taken over the spectrum of a single sample. Mine and vegetation samples were taken from AHI data collected in the field.

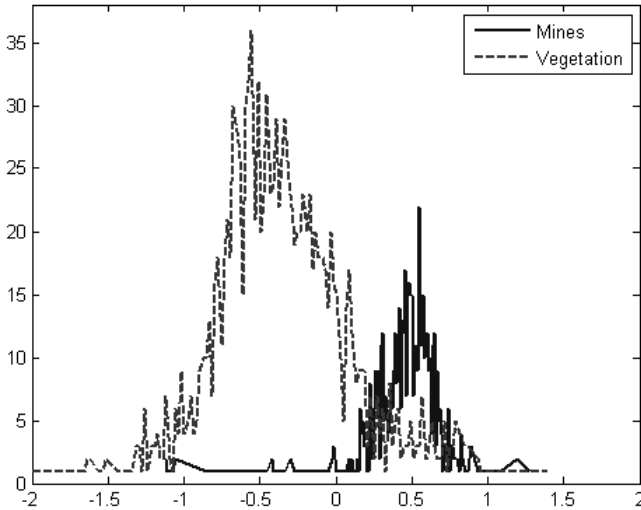


Figure 2. Skewness histogram of mines and vegetation from sample images. The skewness is calculated over wavelength for each mine and vegetation pixel.

B. Calculating Emissivity

In order to compute emissivity statistics for vegetation detection, emissivity must first be computed. Calculating emissivity relies on Planck's function, given by

$$L = \frac{C_1}{\lambda^5 \pi \left[\exp\left(\frac{C_2}{\lambda T}\right) - 1 \right]} \quad (1)$$

where L is irradiance, λ wavelength, T surface temperature and C_1 and C_2 are constants. Emissivity is defined as

$$\epsilon_j = \frac{L_j}{L_{BB}} \quad (2)$$

where j corresponds to the wavelength and L_{BB} is the irradiance of a blackbody. Therefore, in order to accurately calculate either surface temperature or emissivity, the other must be known [3].

Apparent emissivity is the emissivity calculated without adjustments made for atmospheric and environmental effects or if an estimated surface temperature is used. Several methods exist for estimating apparent emissivity with unknown surface temperature [1-4]. We make the assumptions that there are not any major atmospheric effects and the reference temperature is correct. The Emissivity Normalization and Alpha Residuals methods for emissivity calculations [3,4] were both considered. Emissivity Normalization is preferred here since we are able to search for both a low standard deviation and a high mean in the emissivity curve whereas the Alpha Residuals method calculates only relative emissivity values.

III. VEGETATION MAPPING

The vegetation mapping algorithm creates a vegetation map by clustering vectors of emissivity statistics, identifying a vegetation cluster, and setting the blackbody feature to a distance value from each pixel to the vegetation cluster center.

The first step in calculating the blackbody feature is calculating the apparent emissivity values at every pixel in a LWIR image using Emissivity Normalization. We denote the apparent emissivity by

$$\mathbf{e}(x, y) = (e^1(x, y) \ e^2(x, y) \ \dots \ e^{N_B}(x, y))^T \quad (3)$$

where N_B is the number of hyperspectral bands. Note that (3) refers to the apparent emissivity as opposed to the true emissivity defined in (2).

Feature vectors are then created for every pixel from the apparent emissivity spectral using the mean, standard deviation and skewness of the apparent emissivity over wavelength.

$$\mathbf{f}(x, y) = (\mu(x, y) \ \sigma(x, y) \ k(x, y)) \quad (4)$$

where

$$\mu(x, y) = \frac{1}{N_B} \sum_{j=1}^{N_B} e^j(x, y),$$

$$\sigma(x, y) = \sqrt{\frac{1}{N_B - 1} \sum_{j=1}^{N_B} (e^j(x, y) - \mu(x, y))^2},$$

$$k(x, y) = \frac{1}{N_B} \sum_{j=1}^{N_B} \left(\frac{e^j(x, y) - \mu(x, y)}{\sigma(x, y)} \right)^3.$$

The features are then used to cluster the pixels of the image using the Expectation Maximization (EM) algorithm [5]. The EM algorithm is used to estimate the parameters of a Gaussian Mixture with N_C Gaussians using full covariance matrices.

$$p(\mathbf{f}) = \sum_{i=1}^{N_C} p(\mathbf{f} | C_i) w_i \quad (5)$$

where w_i is the probability of class i and $p(\mathbf{f} | C_i)$ is the normal distribution $N(\boldsymbol{\mu}_i, \boldsymbol{\Sigma}_i)$. In our experiments, $N_C = 6$ based on informal experiments with one image. Future work should include identifying the number of clusters adaptively.

All covariances are initialized to the identity matrix. The means are initialized with image pixels. The initial means for the Gaussian mixture are chosen so that there are two small, two medium and two large mean emissivity values selected from the images pixels.

After clustering, the i^{th} cluster, C_i , is represented by mean vector, $\boldsymbol{\mu}_i$, and covariance matrix, $\boldsymbol{\Sigma}_i$. Notice that the components of the mean vector are the average emissivity mean, standard deviation and skewness over the cluster, i.e.,

$$\mathbf{\bar{\mu}}_i = (\mu_{\mu}^i \quad \mu_{\sigma}^i \quad \mu_k^i)^T \quad (6)$$

One cluster, C_B , is chosen to represent the blackbody cluster. This cluster is chosen by

$$C_B = \begin{cases} C_i & \text{if } \arg\max_{C_i} (\mu_{\mu}^i) = \arg\min_{C_i} (\mu_{\sigma}^i) \\ \emptyset & \text{otherwise} \end{cases} \quad (7)$$

Note that we are not guaranteed to find a cluster that satisfies the first condition in (7). In those cases, a blackbody cluster is not found.

The blackbody membership image, v , values are defined to be inversely related to the Mahalanobis distance to the blackbody cluster:

$$v(x, y) = \begin{cases} 0 & \text{if } C_B = \emptyset \\ \frac{1}{1 + \sqrt{(f(x, y) - \mu_B)^T \Sigma_B^{-1} (f(x, y) - \mu_B)}} & \text{otherwise} \end{cases} \quad (8)$$

The blackbody membership image is enhanced using a 3x3 local maximum filter [6] producing the blackbody feature image.

$$V(x, y) = 1 - \text{localmax}(v(x, y)) \quad (9)$$

IV. DETECTION ALGORITHMS

The generated blackbody feature images are used to mask out false alarms in the output of a multi-sensor, multi-algorithm fusion process. A collection of detection algorithms each attempt to detect individual mines while a fusion algorithm increases the probability of detection of individual mines while minimizing false alarms.

Since vegetation mapping is used to reduce false alarms, a possible disadvantage is that a mine may be hidden by vegetation and rejected by vegetation mapping. However, in this case, the detector could have detected the vegetation and did not detect the mine.

The detection algorithms were developed by either the authors or other researchers who provided detection images and associated alarms. Most of these algorithms have been published and are well known. These algorithms are referenced and discussed only briefly here. Following this, we will fully specify a detection algorithm that was developed by the authors and is previously unpublished. All detection algorithms are discussed below [7-12].

The four detectors applied to the imagery are the RX detector originally defined by S. Reed and X. Yu [9], the Fully Constrained Least Squares detector (FCLS) [10,11], the Reststrahlen detector, and the Stochastic Hit-Miss transform defined in [12]. These detectors were selected from a larger set of potential algorithms based on performance and redundancy. Other than the Reststrahlen detector, all of these detection algorithms have been previously published.

RX was applied to detect buried mines and is an implementation of the well-known anomaly detection algorithm provided by Winter [8]. The spectral signature based FCLS detector was implemented and run by Broadwater et al. [10, 11] which requires prior target spectral information. This prior spectral information was one pixel selected from training data. The Stochastic Hit-Miss detector [12] uses random set theory to detect shapes with random parameters.

The Reststrahlen Ratio detector was designed by the authors to detect recently disturbed earth. This feature takes advantage of the Reststrahlen effect which occurs in approximately 8 to 11 microns depending on soil composition. This effect occurs due to properties in recently disturbed soil which causes them to reflect energy in this spectral range. The mirror-like reflectance has a scattering effect which causes a trough in radiance and emissivity [19]. This trough is apparent in our data from recently buried mines at 8.1 to 9.5 microns as depicted in Fig. 3.

The first step of the Reststrahlen Ratio detection algorithm is to select two groups of bands from the input LWIR image. One group, R , consists of bands in the Reststrahlen region (uniformly spaced between 8.87 to 9.40 microns) and the other, N , from bands outside the Reststrahlen region (uniformly spaced between 10.9 to 11.5 microns). The radiance values from each group are averaged as shown below.

$$R(x, y) = \frac{1}{11} \sum_{b=20}^{30} f^b(x, y) \quad (10)$$

$$N(x, y) = \frac{1}{11} \sum_{b=60}^{70} f^b(x, y)$$

where $f^b(x, y)$ denotes radiance at (x, y) in band b . The second step of the Reststrahlen Ratio detection algorithm is to calculate the Reststrahlen ratio feature, S .

$$S(x, y) = \frac{1}{1 + e^{C(x, y)}} \quad (11)$$

$$\text{where } C(x, y) = \frac{R(x, y) - N(x, y)}{\frac{1}{P} \sum_{(u, v)} R(u, v) - N(u, v)} \quad (12)$$

and P is the number of pixels in the image. $C(x, y)$ is the difference (at point (x, y)) of the radiance values in the Reststrahlen region and the non-Reststrahlen region scaled by the average difference in an entire image. Note that the value of S increases as the value of C decreases.

The final step of the Reststrahlen Ratio detection algorithm is local background removal resulting in the detection image.

V. FUSION

Surface mines and buried mines are detectable primarily in different types of imagery, although evidence of both buried and surface mines may exist in both image types. Fusion is difficult since there is often not an alarm from a single mine in both image types. Logical AND fusion will miss many mines and logical OR fusion will produce many false alarms. The best combination of detector outputs is not obvious.

The Choquet integral [12-15] provides a general representation of fusion operators, including voting, linear combinations of order statistics and many others. Detector fusion was performed using the Choquet integral. Descriptions of the integral are plentiful in the literature and are not given here. For our purposes, it suffices to say that the Choquet integral is a trainable, parameterized nonlinear mapping from detector outputs to an output confidence value. The parameters are called measures. In our experiments, Choquet integrals were trained with unconstrained measures. Vegetation mapping was incorporated by multiplying the blackbody feature by the Choquet integral confidence.

VI. DATA

This paper examines Lynx and Mirage SARs and Airborne Hyperspectral Imager (AHI) HSI data acquired at an arid testing site. The Lynx flew in a fixed wing aircraft at altitudes around 2590m, and the AHI flew in a fixed-wing aircraft at 304m and 610m. The Lynx SAR is a narrow band, Vertically-transmitted, Vertically-received (VV) polarized SAR deployed in spotlight mode in order to achieve 10.16cm resolution on the ground. The Lynx SAR operates over 16.7 GHz. The Mirage SAR is broad band and operates over the band 250MHz to 3000MHz. Unlike the narrow band Lynx SAR, the

broad band SAR can penetrate the ground's surface. The use of both of these types of SARs allows detection of mines at different depths. The AHI sensor has spatial resolutions of 15.24cm x 35.56cm at 304m, and 30.48cm x 35.56cm at 610m. AHI has 256 bands from 7.89 to 11.49 microns with a spectral resolution of 100 nm. These bands are binned and trimmed to 70 bands over the same range.

Landmines were placed in a grid with 5m spacing, and within this area, fiduciary aluminum top hat markers were placed in a grid with 20m spacing. The fiduciary aluminum top hat markers are metal objects that appear bright in the imagery. They are used during the alignment and ground truthing process. A semi-automated fiducial detection algorithm [7] was used to assign ground coordinates to each target. Typical errors in ground coordinates were less than a target size.

The lanes are graded strips and are free of vegetative clutter. The "spaces" consist of the natural desert varnish malapai, and contain washes with vegetation ranging from the size of a landmine to a 4.6m palo verde tree or saguaro cactus.

Figure 3 shows false color AHI imagery at 1000' AGL over the site. The Red channel of the false color image holds radiance at 8.14 μm which is just before the Reststrahlen peak; the Green channel is set to 8.93 μm at the beginning of the Reststrahlen peak, and Blue is set to 10 μm which is just at the tail end of the peak. With this color scale, one would hope that disturbed earth, associated with buried mines, generally appears cyan, malapai reddish, and vegetation white because of its neutral spectrum. However, as can be seen, the difference between the cyan and white can be very subtle and sometimes vegetation can appear cyan as well. In addition, the SAR detection algorithms can produce alarms at the locations of the shrubs.

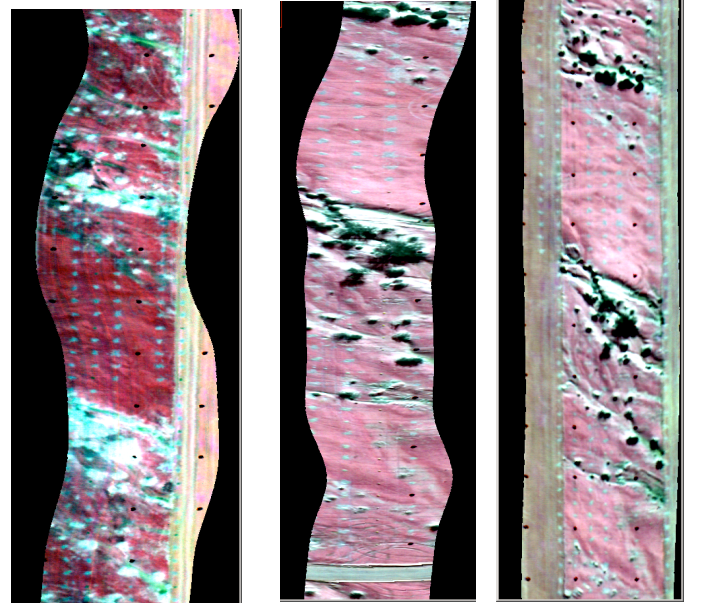


Figure 3. Airborne AHI imagery over the arid site; R = 8.14 μm , G = 8.93 μm , B = 10.0 μm

A typical SAR image over the site is shown in Figure 4. Note the high response to vegetation.



Figure 4. Narrowband SAR image over the arid site.

VII. EXPERIMENTS AND RESULTS

Experiments were performed using overlap regions. Overlap regions are areas where SAR and AHI imagery overlap. Points Of Interest (POIs), which are alarm GPS coordinates, were given by each detector. Only POIs within an overlap region are kept. The POIs from different detection algorithms were merged by linking nearby POIs. In addition, if only a subset of the detectors produced the same POI, then the GPS coordinates were used to collect confidence values from the other detection algorithms and the blackbody feature image. The confidences from all of the detection algorithms and the blackbody feature image define a confidence vector for each POI.

There are four mine types, two plastic-cased (PC1 and PC2) and two metal-cased (MC1 and MC2). Mine distributions are shown in Table 1. Eight images were used: five AHI, two broad band SAR and one narrow band SAR.

TABLE 1. MINE DISTRIBUTION FOR THE OVERLAP REGIONS

		Narrow-band SAR / AHI	Broad-band SAR / AHI
Mine	Depth	Quantity	Quantity
PC1	10 cm	72	90
MC1	10 cm	134	124
MC1	Flush	87	119
MC1	Surface	49	73
MC2	Surface	42	72
PC2	Surface	5	5
Total		389	483

Fusion was performed using a MEAN operator and Choquet

integrals with respect to optimal full measures. The MEAN operator was chosen for comparison because it performed the best of the simple fusion operators (among logical and soft AND and OR). To evaluate the effect of vegetation mapping, each experiment was performed with and without the Blackbody feature.

Cross-validation testing was performed. The POIs from one overlap region were tested while POIs from other overlap regions with the same types of images were used for training. Each of the overlap regions was used as the test set once. Each POI in the test set was assigned a confidence by either the MEAN operator, the MEAN operator multiplied by the Blackbody feature, the Choquet integral trained on the corresponding training set, or the latter multiplied by the Blackbody feature. The set of all such confidences from all overlap regions were used to compute Probabilities of Detection (PD) and False Alarm Rates (FARs). For a given threshold, PD is defined as the number of mines with confidence above the threshold divided by the number of mines. FAR is the number of non-mines above the threshold divided by the number of square meters. For satisfactory minefield detection, we would like PDs of at least 50-60% and FARs between 0.001 and 0.01 [7].

The fusion results from narrow band and broad band SAR / AHI are shown in Tables 2 and 3, respectively. Each column in each table represents a probability of detection. The first two rows of each table show the FARs for the corresponding PDs for MEAN fusion with and without the blackbody feature. The third rows show the percent reduction in FAR achieved using the blackbody feature. The fourth rows show the FARs for the corresponding PDs for Choquet integral fusion without the blackbody feature. The fifth and sixth rows show the FARs for the corresponding PDs of the Choquet integral fusion using the blackbody feature. The fifth rows used a blackbody feature that was created without the use of skewness information; whereas, the sixth rows used this information during the clustering process in the creation of the blackbody feature. The last rows show the percent reduction in FAR achieved using the Blackbody feature constructed with the skewness information in comparison to the Choquet integral fusion without the blackbody feature.

TABLE 2. BROAD BAND SAR TABLE FAR REDUCTION USING BB FEATURE

	PD				
Fusion	20%	30%	40%	50%	60%
MEAN	6.0E-4	2.0E-3	4.0E-3	5.5E-3	1.2E-2
MEAN w/ BB	2.5E-4	8.0E-4	2.0E-3	3.1E-3	8.0E-3
FAR Red.	58.3%	60.0%	50.0%	43.6%	33.3%
Choquet	1.4E-3	3.0E-3	4.9E-3	6.7E-3	1.2E-2
Choq. no skew	1.5E-3	3.8E-3	1.0E-2	1.9E-2	3.1E-2
Choq. w/ BB	1.6E-4	1.0E-3	2.4E-3	4.0E-3	7.1E-3
FAR Red.	88.6%	66.7%	51.0%	40.3%	40.8%

TABLE 3. NARROW BAND SAR TABLE FAR REDUCTION USING BB FEATURE

	PD				
Fusion	20%	30%	40%	50%	60%
MEAN	3.7E-3	6.2E-3	9.2E-3	1.2E-2	1.9E-2
MEAN w/ BB	2.0E-3	2.8E-3	4.3E-3	7.1E-3	1.1E-2
FAR Red.	46.0%	54.8%	53.3%	40.8%	42.1%
Choquet	7.6E-4	1.2E-3	3.0E-3	6.2E-3	1.2E-2
Choq no skew	1.0E-3	7.1E-3	9.2E-3	2.0E-2	3.4E-2
Choq w/ BB	2.0E-4	4.2E-4	1.3E-3	3.7E-3	8.0E-3

FAR Red.	73.7%	65.0%	56.7%	40.3%	33.3%
-----------------	--------------	--------------	--------------	--------------	--------------

Creating the blackbody feature using the skewness information drastically reduced the false alarm rate of the fusion algorithm. The inclusion of the skewness aided in distinguishing between vegetation and other materials. Most notably, the skewness information helped differentiate between landmines and vegetation. The incorporation of the Blackbody feature created without skewness information caused landmines to be mistaken for vegetation. Subsequently, many mines were unable to be detected.

Vegetation mapping which used the skewness information improved all fusion results. At higher false alarm rates, the reduction in FARs is not as substantial but significant nonetheless. This decrease occurred because mines concealed by vegetation were found at high FARs since the vegetation produced a FA in the vicinity of the mine. In this case the algorithm is mistaking vegetation for a mine and getting a “lucky” detection. Eliminating numerous FAs is more important in minefield detection than keeping lucky detections.

An example image and the corresponding vegetation mask is shown in Figure 5. Figure 5 shows the original image at around 8.92 microns on the left. Note that the image is warped due to aircraft motion. Landmines appear in rows (although this information is not used in the algorithm since it is not necessarily true). Figure 5(b) shows the vegetation map. Dark values indicate vegetation. The contrast between mines and vegetation has been enhanced, even though they share some spectral characteristics, resulting in the reduced false alarm rates reported in the tables.

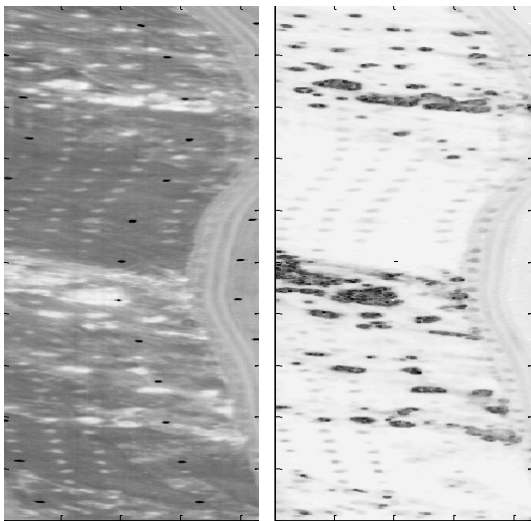


Figure 5. LWHSI image and corresponding vegetation mask.

VIII. CONCLUSIONS

Vegetation mapping proved useful in eliminating false alarms in the area of landmine detection. It has been widely accepted that mean and standard deviation of emissivity is useful in vegetation detection in the LWIR. The inclusion of skewness information has been shown in our experiments to improve vegetation mapping by providing more distinction between vegetation and background materials.

In the future, we will attempt to discriminate between different vegetation types. Our algorithm reduced false alarms by identifying trees, bushes, and other thick vegetation. However it is important to differentiate between thick vegetation and grass. Mines placed in grassy fields are detectable by mine detection algorithms. In this case, masking out the portion of the image containing vegetation would remove detectable mines. If we could differentiate between types of vegetation, this problem could be avoided and this scheme could be applied to a wider range of environments. The literature indicates that there are physical differences between thick and light vegetation in the LWIR [1]. Therefore integration of these physical properties to the algorithm may be possible.

ACKNOWLEDGMENTS

Research was sponsored by the U. S. Army Research Office and U. S. Army Research Laboratory and was accomplished under Cooperative Agreement Number DAAD19-02-2-0012. The views and conclusions contained in this document are those of the authors and should not be interpreted as representing the official policies, either expressed or implied, of the Army Research Office, Army Research Laboratory, or the U. S. Government. The U. S. Government is authorized to reproduce and distribute reprints for Government purposes notwithstanding any copyright notation hereon. The authors thank William Clark of ARO and Michael Cathcart of Georgia Tech for their support of this research.

REFERENCES

- [1] A. N. French, T. J. Schmugge, and W. P. Kustas, “Discrimination of Senescent Vegetation Using Thermal Emissivity Contrast”, *Remote Sensing of Environment*, Vol. 74, pp. 249-254, 2000.
- [2] E. F. Lambin and D. Ehrlich, “The Surface Temperature – Vegetation Index for Land Cover and Land Cover Change Analysis”, *Int’l J. of Remote Sensing*, Vol. 17, pp. 463-487, 1996.
- [3] P. Kealy and S. Hook, “Separating Temperature and Emissivity in Thermal Infrared Multispectral Scanner Data: Implications for Recovering Land Surface Temperatures”, *IEEE Trans. Geoscience and Remote Sensing*, Vol. 31, No.6, pp. 1155-1164, Nov. 1993.
- [4] D. Gu and A. R. Gillespie, “A New Approach for Temperature and Emissivity Separation”, *Int’l J. of Remote Sensing*, Vol. 21, No. 10, pp. 2127-2132, 2000.
- [5] S. Theodoridis and K. Koutroumbas, *Pattern Recognition*, 2nd ed. San Diego: Elsevier Academic Press, 2003, pp. 36-39.
- [6] R. C. Gonzalez and R. E. Woods, *Digital Image Processing*, 2nd ed. Upper Saddle River: Prentice Hall, 2002, pp. 234-235.
- [7] William C Radzelovage, Personal Communication
- [8] E. Winter, Personal Communication
- [9] X. Yu, I. S. Reed, and A. D. Stocker. “Comparative Performance Analysis of Adaptive Multispectral Detectors,” *IEEE Trans. Signal Processing*, Vol. 41, No. 8, August 1993, pp. 2639-2656.

- [10] D. Heinz and C. Chang, "Fully constrained least squares linear spectral mixture analysis method for material quantification in hyperspectral imagery", *IEEE Trans. Geoscience and Remote Sensing*, Vol. 39, No. 3, March 2001, pp. 529-545.
- [11] J. Broadwater, R. Meth, R. Chellappa, "Hybrid Algorithm for Subpixel Detection in Hyperspectral Imagery", *IEEE Conf. Geoscience Remote Sensing*, Sept. 2004, CDROM.
- [12] P. D. Gader, Wen-Hsiung Lee, and Andres Mendez-Vasquez, "Continuous Choquet Integrals with respect to random sets with applications to landmine detection", *Proc. IEEE Conf. Fuzzy Systems*, Budapest, Hungary, July 2004, CDROM.
- [13] M. Schatten, P. Gader, J. Bolton, A. Zare, A. Mendez-Vasquez, "Sensor fusion for airborne landmine detection" *SPIE Conf. Detection Remediation Technologies for Mines and Minelike Targets*, vol. 6217, April 2006, CDROM.
- [14] P. D. Gader, A. Mendez-Vasquez, K. Chamberlin, J. Bolton, and A. Zare, "Multi-Sensor and Algorithm fusion with the Choquet Integral: Applications to Landmine Detection", *IEEE Conf. Geo-science and Remote Sensing*, Anchorage, AK, September 2004, CDROM.
- [15] A. Mendez-Vazquez, P. D. Gader, J. M. Keller, K. Chamberlin, "Minimum Classification Training for Choquet Integrals with Applications to Landmine Detection", *IEEE Trans. on Fuzzy Systems*, (submitted)
- [16] P.G. Lucey, T.J. Williams, M. Mignard, J. Julian, D. Kobubun, G. Allen, D. Hampton, W. Schaff, M. J. Schlangen, E. M. Winter, W. B. Kendall, A. D. Stocker, K. A. Horton, A. P Bowman, "AHI: An Airborne Long-Wave Infrared Hyperspectral Imager", *Proc. of SPIE*, Vol. 3431, Nov. 1998, pp 36-43.
- [17] General Atomics, *LYNXSAR*, [Online]. Available: <http://www.LYNXSAR.com>
- [18] L.E. Kirkland, K. C. Herr, P. M. Adams, J. McAfee, J. Salisbury, "Thermal Infrared Hyperspectral Imaging from Vehicle-carried Instrumentation", *Proc. of SPIE*, Vol. 4816, 2002, pp 415-425.
- [19] L. Kirkland, K. Herr, E. Keim, P. Adams, J. Salisbury, J. Hackwell, A. Treiman, "First Use of an Airborne Thermal Infrared Hyperspectral Scanner for Compositional Mapping", *Remote Sensing of Environment*, Vol. 80, Feb. 2002, pp. 447-459.